International Journal of Refractory Metals and Hard Materials 128 (2025) 107068

Contents lists available at ScienceDirect

International Journal of Refractory Metals and Hard Materials

journal homepage: www.elsevier.com/locate/IJRMHM

Effects of femtosecond laser surface modified WC and NbC based inserts during the face-milling of automotive Grey Cast Iron (a-GCI)

M. Rabothata [a,b,*], R. Genga [a,b,d,e], N. Mphasha [a,b], K. Phaka [b], N. Nelwalani [c], S. Ngongo [f], C. Polese [b,d,e], S. Huang [g], J. Vleugels [g], P. Zeman [h]

[a] Academic Development Unit, University of Witwatersrand, South Africa
[b] School of Mechanical, Industrial and Aeronautical Engineering, University of Witwatersrand, South Africa
[c] School of Mining, Metallurgy and Chemical Engineering, University of Johannesburg, South Africa
[d] DSI-NRF Centre of Excellence in Strong Materials, University of Witwatersrand, (2004-2023), South Africa
[e] ARUA Centre of Excellence in Materials, Energy and Nanotechnology, University of Witwatersrand, South Africa
[f] CHRTEM, Nelson Mandela University, South Africa
[g] Department of Materials Engineering, KU Leuven, Belgium
[h] RCMT, Czech Technical University, Czech Republic

ARTICLE INFO

Keywords:
Pulsed electric current sintering
Laser surface modification
Face milling
Niobium carbide
Molybdenum
Machining performance
Grey cast iron

ABSTRACT

Rapid pulsed electric current sintering (PECS), TiC, TiC_7N_3 and Mo additions, and femtosecond (fs) laser surface modification (LSM) were used to improve the machining of automotive grey cast iron (a-GCI) using WC and NbC based cemented carbides cutting inserts. Additions of Mo and TiC as well as the use of PECS refined the grain sizes of NbC-12Ni based cermet from ~4.6 μm to ~1 μm, increasing the hardness (by ~3 GPa) and wear resistance. Shark skin (S-LSM) and pyramidal (P-LSM) patterns were introduced to improve the wear and mechanical impact resistance of the cutting inserts. Face milling of a-GCI was performed at 200 m/min cutting speed (V_c), 1.0 mm depth of cut (a_p), and 0.1 mm/tooth feed rate (f). The insert cutting-edge wear and damage were evaluated after every pass using optical microscopy and high angular annular dark field scanning transmission electron microscopy (HAADF-STEM). The machining performance of the cutting inserts was assessed by cutting forces, wear, and cutting insert tool life. The PECS produced NbC-10TiC-12[Ni/Mo] (wt%) P-LSM cutting insert had the lowest flank wear rate (FWR) (1.44 μm/min) after 20 min of machining. In addition, both the S-LSM and P-LSM patterns improved the cutting insert tool life of PECS produced NbC-12[Ni/Mo] (wt%) blank (B) cutting insert by ~300 % and ~ 900 %. Resulting in FWRs reductions of the respective insert from 21.04 μm/min after 2 min of machining to 5.97 μm/min and 1.94 μm/min after 8 min and 20 min. In general, LSM improved the NbC based cutting inserts' tool life and reduced the FWRs.

1. Introduction

The objective of this research was to design, develop, and produce NbC-Ni based cemented carbide inserts as potential cutting inserts for face-milling machining of automotive grey cast iron (a-GCI), which is widely used in automotive applications [1]. Additionally, the study aimed to explore the impact of laser surface modification (LSM) on the performance of these cutting inserts during machining. Cemented carbides are hardmetals consisting of a predominant hard but relatively brittle carbide phase (WC, TiC) and a metallic reinforcement binder (Co, Ni, Fe) [2]. The WC-Co cutting inserts have been reported to exhibit poor chemical stability during the machining of steels and cast irons due to iron's higher affinity for carbon than tungsten [2], resulting in chemical wear and consequently reduced insert tool life. Furthermore, there has been concerns over WC-Co growing supply risks and unstable market prices [3]. Hence, alternatives such as NbC have been investigated [4]. Niobium carbide has a lower solubility in steels and cast irons than WC [5], slightly lower room temperature hardness than WC, but a significantly higher melting temperature. In addition, NbC has better high-temperature properties to WC and lower density [3,4]. Nickel can improve hot hardness and resistance to thermal cracking in NbC-based cermets [6]. Molybdenum has been reported to improve the wetting behavior of the binder during sintering [7]. This improved wettability creates a diffusion gradient through the liquid-solid interface enables

* Corresponding author at: Academic Development Unit, University of Witwatersrand, South Africa.
E-mail address: Mahlatse.Rabothata@wits.ac.za (M. Rabothata).

https://doi.org/10.1016/j.ijrmhm.2025.107068
Received 15 October 2024; Received in revised form 18 January 2025; Accepted 18 January 2025
Available online 20 January 2025

Mo to diffuse freely into the carbide phase. Consequently, leading to a reduction in interfacial energy during sintering, and improving the bonding between the carbide and binder phases [2]. Furthermore, the addition of Mo has been linked to improved material's hardness properties, and densification [2]. Laser surface modification (LSM) has proven to be a highly effective technique for improving the machining performance of cutting inserts, particularly those made from hard engineering materials like cemented carbides [4]. By introducing microfeatures through processes such as laser ablation, LSM allows for sophisticated surface texturing or patterning and complex shaping that are challenging to achieve using conventional machining methods. The LSM technology has advanced over time, from nanosecond to femtosecond laser systems, enabling the creation of high-quality, precise patterns across large surface areas without causing thermal damage [8]. The LSM has been shown to reduce friction at contact areas, enhance chip evacuation, and improve heat dissipation during high-speed or dry machining, all of which contribute to increased cutting efficiency and extended tool life. Additionally, LSM enhances critical mechanical properties such as fatigue life, thermal stability, fracture toughness, and hardness, making cutting inserts more resistant to abrasive wear and deformation. The use of femtosecond (fs) lasers allows for unparalleled precision in tailoring surface textures, leading to improved performance, dimensional accuracy, and long-term durability in demanding machining conditions [9]. In this study, pulsed electric sintering (PECS), additions of Mo as a partial binder replacement, and TiC and TiCN as secondary hard phases, and fs-LSM were used to improve the machining performance of NbC-Ni cutting inserts during face-milling of a-GCI. For this purpose, cutting inserts with various compositions were produced via liquid phase sintering (LPS) and PECS techniques. The surfaces of the insert cutting edges were modified using fs lasers to create shark skin (S) and pyramid (P) based micro-patterns. The combined effects of composition, sintering methods, and surface texturing on the machining performance of the cutting inserts were then explored. The influence of specific elements and the sintering approaches was examined in the unmodified (blank) inserts, whereas the impact of LSM was evaluated on treated inserts. The interplay between these variables was investigated to better understand the performance of the enhanced WC and NbC based cutting inserts.

2. Experimental procedure

2.1. Starting powders

The starting powders and their characteristics are in Table 1. The powders were homogeneously mixed in 99 % pure ethanol for 48 h in a multi-directional mixer using WC milling balls. After the milling process, the wet powders were then dried for one hour with a rotavaporizer operating at the speed and temperature of 80 rpm and 75 °C, respectively.

2.2. Sintering

The milled and dried powders were cold isostatically pressed (EPSI, Belgium) into green compacted powder cylinders at a pressure of 200 MPa. The compacted powder cylinders of various compositions were consolidated in the LPS (HP, W100/150–2200-50 LAX, FCT Systeme, Frankenblick, Germany) and PECS ((HP D5, FCT Systeme, Germany) furnaces. During LPS, different sintering profiles were used according to the powder compositions (Table 2). For example, WC-10TiC-10Co (wt %) compacts were first heated to 1050 °C in a dynamic vacuum environment (~10 Pa) at an initial heating rate of 10 °C/min. Subsequent heating of compacts to 1250 °C was carried out at a heating rate of 5 °C/min. The compacts were then further heated until a temperature of 1390 °C was reached at a heating rate of 3 °C/min. Sintering was then performed at this temperature for 90 min without any external applied pressure. The furnace was then cooled to room temperature at a rate of 3 °C/min. Irrespective of their compositions, the PECS samples were consolidated using similar sintering profiles. The powder compacts were first heated to 1050 °C in a vacuum atmosphere at a pressure of ~2 Pa and 200 °C/min heating rate. They were further heated to 1285 °C at a slower heating rate of 50 °C/min, and then rapidly sintered at this temperature for 10 min at 30 MPa. Finally, the samples were cooled to room temperature at a rate of 200 °C/min. The powders were separated from the die and punch assembly using horizontal and vertical graphite papers. Diffusion of carbon from the graphite paper into the powder during sintering was prevented by applying hexagonal boron to the graphite paper. A carbon cloth was wrapped around the graphite dies to minimise heat loss from the surface of the die. The temperature was monitored and controlled by an optical pyrometer aimed at a central hole on the anode (upper punch), ~ 1 mm above the surface of the sample to optimise the accuracy of the sample temperature [10]. The displacement of the plunger was used to monitor the consolidation of the powder compacts in the axial direction.

2.3. Material characterisation

The density of the sintered samples was determined according to the Archimedes principle using an ED224S density measuring machine (Sartorius, Germany). The microstructures of the cemented carbides were examined using field emission electron microscopy (SEM) (Sigma VP, Zeiss, Germany) in both electron backscattered diffraction (BSE) and secondary electron (SE) mode, which were respectively used to identify and quantify elemental composition through energy dispersive X-ray spectroscopy (EDS), and to obtain morphology and surface topology of the samples. The mean carbide grain sizes of the sintered samples were determined using the line intercept technique using SEM-BSE micrographs in ImageJ software. The random straight lines were drawn through the micrographs, the number of grain boundaries intersecting the lines were counted, and the average grain sizes were then found by dividing the number of intersections by the actual line length. High resolution transmission electron microscopy (HRTEM) and high angular annular dark-field scanning transmission electron microscopy (HAADF-STEM) (JEOL ARM—200F, JEOL, Japan) were used to analyse the grain interfaces and compositional variations within the microstructure. The samples used for determining Vickers hardness (HV_{30}) and fracture toughness (K_{IC}) were prepared using the standard metallographic preparation procedure. The HV_{30} was measured by applying a force of 30 N for 10 s with a diamond indenter on the AVK-CO testing machine

Table 1
Starting powders specifications.

Materials	Particle size (μm)	Crystal structure	Source
WC	1–2	HCP	Umicore, Belgium
Co	0.55	HCP	Umicore, Belgium
Ni	3–7	FCC	Vale, UK
Mo	5	BCC	Plansee, Chile
TiC_7N_3	3	FCC	H.C. Starck, Germany
TiC	1–1.5	FCC	H.C. Starck, Germany
NbC	1–1.75	FCC	CBMM, Brazil

Table 2
Sample composition and sintering profile.

Composition (wt%)	Sintering technique	Dwelling time (min)	Temperature (°C)
WC-10TiC-10Co	LPS	90	1390
NbC-12[Ni/Mo]	LPS	90	1390
	PECS	10	1285
NbC-10TiC-12Ni	PECS	10	1285
NbC-10TiC-12[Ni/Mo]	PECS	10	1285
NbC-10TiC_7N_3-12Ni	LPS	90	1450
	PECS	10	1285

(Mitutoyo Akashi, Japan) and taking the average of five indentations at different locations on each sample. Fracture toughness was calculated according to Shetty's Eq. [11] using the radial cracks produced by the diamond indenter following hardness measurements. The criteria of $c/a \leq 2.25$ and $0.25 \leq l/a$ 2.5 were satisfied during the K_{IC} calculations, where c is the crack length measured from the centre of the indentation to the crack tip, a is the half diagonal of the indentation, and l is the distance between c and a. The elastic modulus and shear modulus were determined using an Olympus 45MG pulse-echo tester (Olympus Corporation, Japan) by measuring the samples' wave sound velocities in the shear and longitudinal directions.

2.4. Cutting inserts production and Laser surface modification (LSM)

The cutting inserts were initially cut out to dimensions 12.7 mm × 12.7 mm × 5 mm from both LPS and PECS disc samples (Ø50mm x 5 mm), using a Fanuc Robocut α-O1A electro-discharge machine (EDM) wire cutting machine. This was followed by lapping and grinding of the inserts to a thickness of ~4.3 mm and a nose radius of 1.6 mm according to SNMA shape using a Peter-Wolters 3R-1200 (Peter Wolters, Germany) lapping machine and an EWAG RS12 Edge profile grinder (EWAG, Switzerland) to chamfer-hone the inserts to a radius of 0.2 mm and a chamfer angle of 20°. A Medicom LD50C femtosecond laser (Medicom, Czech Republic) with a maximum power output of 50 W was used to modify the surface of the cutting inserts by creating S-LSM and P-LSM micro-patterns on the cutting edges. The micro-patterns were created by applying an 8 μJ pulse energy with a repetition rate of 200 Hz. The scanning speed of 600 mm/s and laser the spot size of 30 μm were used at a pulse overlap of 90 %. The processing time for both patterns was 293 s.

2.5. Face-milling machining tests

The WC- and NbC- based cutting inserts were secured on a Pilot F75SN12080 cutting tool holder (Pilot Tools, South Africa) attached to a semi-automatic MAHO MH70 (MAHO, Germany) milling machine. The a-GCI workpieces of dimensions 160 mm × 160 mm (square) x 30 mm (thick) were provided by Auto Industrial Group (Pty) Ltd. who are a prominent supplier of automotive components in South Africa. The parameters used for the milling tests are given in Table 3. The radial depth of cut (a_r) was 80 mm (defined by the diameter of the cutting tool holder. All tests were performed under dry milling conditions. A Kistler Multicomponent Force Dynamometer (Kistler, Switzerland) was attached to the workpiece clamping vice to measure the cutting forces in the longitudinal (F_x), transverse (F_y) and vertical (F_z) directions. The resultant force (F_i) was calculated using Eq. 1.

$$F_i = \sqrt{F_x^2 + F_y^2 + F_z^2} \tag{1}$$

The average resultant force (F) is then calculated using Eq. 2.

$$F = \left(\sum F_i\right)/N \tag{2}$$

where, $\sum F_i$ is the sum of all the resultant forces, $i = 1, 2, \ldots, N$ and N is the total number of the resultant forces. The cutting inserts wear and edge failure were assessed after every machining pass using Nikon D5000 (Nikon, Japan) optical microscopy. Additional analyses of wear were done using the same techniques as material characterisation. The insert tool life was determined by the ISO-3685:1993 standards [12]. Accordingly, the criteria for failure were VB_{max} (maximum flank wear length) ≥ 300 μm, or a shattered, chipped, or badly grooved cutting edge. The flank wear rate (FWR) was calculated using Eq. 3 [2].

$$FWR = VB_{max}/t \tag{3}$$

where, t is the cutting time.

Table 3
Face-milling parameters.

Cutting speed (V_c) [m/min]	Depth of cut, (a_p) [mm]	Spindle speed, (n) [rpm]	Feed (f) [mm/tooth]	Material removal rate ($\dot{m}_r$) [mm^3/min]
200	1.0	800	0.1	6400

3. Results and discussion

3.1. Densification

All the sintered samples, irrespective of the sintering process, had relative densities of above 97 % as shown in Table 4. The addition of Mo as a binder phase to the NbC-12Ni (wt%) composition had negligible effect on the densification of the NbC-12[Ni/Mo] (wt%) sample [13]. However, a contrasting observation was observed in the NbC-10TiC-12Ni (wt%) and NbC-10TiC-12[Ni/Mo] (wt%) samples, whereby the addition of Mo slightly improved the densification. Here, Mo addition improved the wettability of the binder phase to the hard TiC phase by the formation (Nb, Ti, Mo) C solid solution which is wetted easier by Ni liquid than TiC [14]. Similar observations of this phenomenon were made elsewhere [15]. The additions of TiC and TiC_7N_3 to the NbC-12Ni (wt%) slightly inhibited the densification of PECS produced NbC-10TiC-12Ni (wt%) and NbC-10 TiC_7N_3-12Ni (wt%) samples at 1285 °C and 30 MPa, respectively. These was because both TiC and TiC_7N_3 have relatively higher melting points than NbC, thus their presence adversely impacted densification during the sintering process [2,16]. As a result, higher sintering temperatures and pressures were required [17].

3.2. Microstructure

The LPS WC-10TiC-10[Co/Mo] (wt%) sample had finest grain sizes compared to all the NbC samples. Fig. 1 shows the SEM-BSE and HAADF-STEM micrographs of the LPS WC-10TiC-10[Co/Mo] (wt%). As shown in Fig. 1, the microstructure of WC-10TiC-10[Co/Mo] (wt%) exhibited fine WC platelet shaped grains (light phase) with homogeneously distributed Co binder pools (light grey phase), dark grey phase is the (W, Ti, Co) C solid solution and TiC rich solid solutions (dark phase).

The fine WC grains were due to the addition of TiC and the partial substitution of Co by Mo. The presence of Mo in the microstructure improved wettability between the TiC and metallic Co phase leading to the formation of (W, Ti, Mo, Co) C solid solution which limited grain boundary migration and slowing down the aggregation of WC grains during sintering [15,18]. Although Mo improves the wettability between the ceramic phase and the metallic phase, it also reduces the solubility of TiC in the binder, thus limiting grain growth by the solution-precipitation mechanism during sintering [18]. This effect was confirmed by the presence of a dark undissolved TiC phase as shown in Fig. 1 (a). Furthermore, as expected, the additives also resulted in the change of shape of the WC grains, yielding a microstructure that has a mixture of thin platelets (elongated rectangular), faceted and near-spherical smaller grains as opposed to truncated trigonal prism shaped

Table 4
Sintered samples densification and mean carbide sizes.

Sample Composition (wt%)	Densification (%)	Mean carbide size (μm)
WC-10TiC-10Co (LPS)	98.36 ± 0.170	1.02 ± 0.08
NbC-12[Ni/Mo] (LPS)	98.48 ± 0.372	2.52 ± 0.09
NbC-12[Ni/Mo] (PECS)	98.54 ± 0.054	1.49 ± 0.48
NbC-10TiC-12Ni (PECS)	97.82 ± 0.032	1.62 ± 0.12
NbC-10TiC-12[Ni/Mo] (PECS)	98.14 ± 0.053	1.35 ± 0.06
NbC-10TiC_7N_3-12Ni (LPS)	98.01 ± 0.079	2.97 ± 0.23
NbC-10TiC_7N_3-12Ni (PECS)	97.63 ± 0.055	1.68 ± 0.15

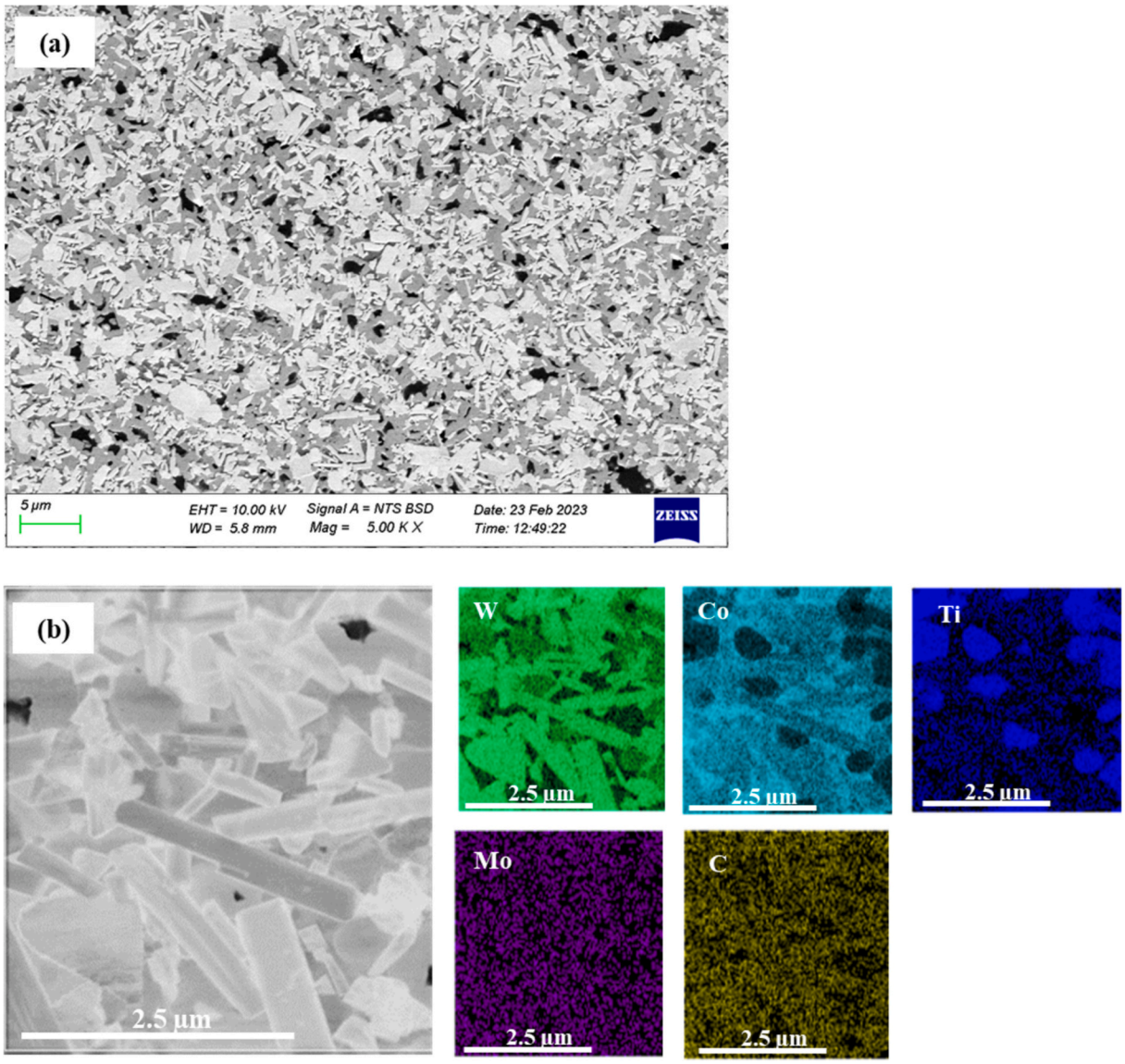

Fig. 1. SEM-BSE image of (a) LPS produced WC-10TiC-10[Co/Mo] (wt%) sample showing WC (light), Co (light grey), (W, Ti, Co) C solid solution (dark grey), and TiC- rich (dark) phases, and (b) HAADF-STEM images of WC-10TiC-10[Co/Mo] (wt%) (T1ML) sample produced by LPS showing: WC (green), Co (cyan), Ti (blue), Mo (purple) and C (yellow). (For interpretation of the references to colour in this figure legend, the reader is referred to the web version of this article.)

found in the WC-Co alloys [19]. Molybdenum was not detected in EDS due to the small amount of its content but was found to be all over the microstructure of WC-10TiC-10[Co/Mo] (wt%) sample by HAADF-STEM mapping (see Fig. 1 (b)). The HAADF-STEM mapping indicated that the TiC phase was isolated from the WC-Co composition. This was mainly due to the lower sintering temperatures and pressures which prevented a complete dissolution of TiC, leading to the formation of Ti-rich regions [20]. In other areas of the microstructure, the fine TiC precipitated into WC-Co phase leading to the formation of the (W, Co, Ti) C solid solution [20]. The mapping also revealed that the Co binder phase typically coincided with the WC grains, especially along the boundaries of the carbide. This was due to the good solubility of WC in Co and the good wetting of WC by Co [2].

Fig. 2 shows the SEM-BSE images of NbC-Ni based samples. The LPS produced NbC-Ni based samples had slightly larger NbC grains (light phase) and homogeneously distributed Ni binder (medium dark phase) compared to their PECS samples (see Fig. 2). This was due to slightly higher sintering temperatures and longer sintering times than during PECS [4,5]. The larger NbC grains in LPS samples were due to the grain growth by coalescence and Ostwald ripening [21]. The better Ni pool distribution was attributed to the formation of a liquid phase during LPS, unlike in PECS where the Ni liquid only formed momentarily and then followed by rapid solidification [5]. In addition, the microstructures of the PECS samples exhibited fine grains with NbC skeleton network due to shorter sintering time and lower sintering temperature associated with PECS process [22]. As shown in Fig. 2, the microstructures also exhibited pores (sub-micron) dark spherical spots inside the NbC grains) [23,24]. The presence of pores in the samples could be attributed to the local lack of Ni during solid state sintering which favoured the coalescence of NbC clusters by grain boundary migration and entrap pores, before the liquid phase was formed [24]. In general, porosity in the microstructure typically suggests that the densification process was adversely impacted [25]. The effects of the additions of Mo, TiC, TiC_7N_3 and Mo plus TiC, to the NbC-12Ni (wt%) composition were investigated in PECS produced samples. These additions have been reported to influence the microstructure of NbC-Ni based cermets. For example, the addition of Mo or Mo_2C can inhibit grain growth by improving the wettability of NbC during solid state sintering [23]. In addition, grain growth can also be restricted through the formation of (Nb, Mo) C solid solution which delays the aggregation of NbC grains during sintering

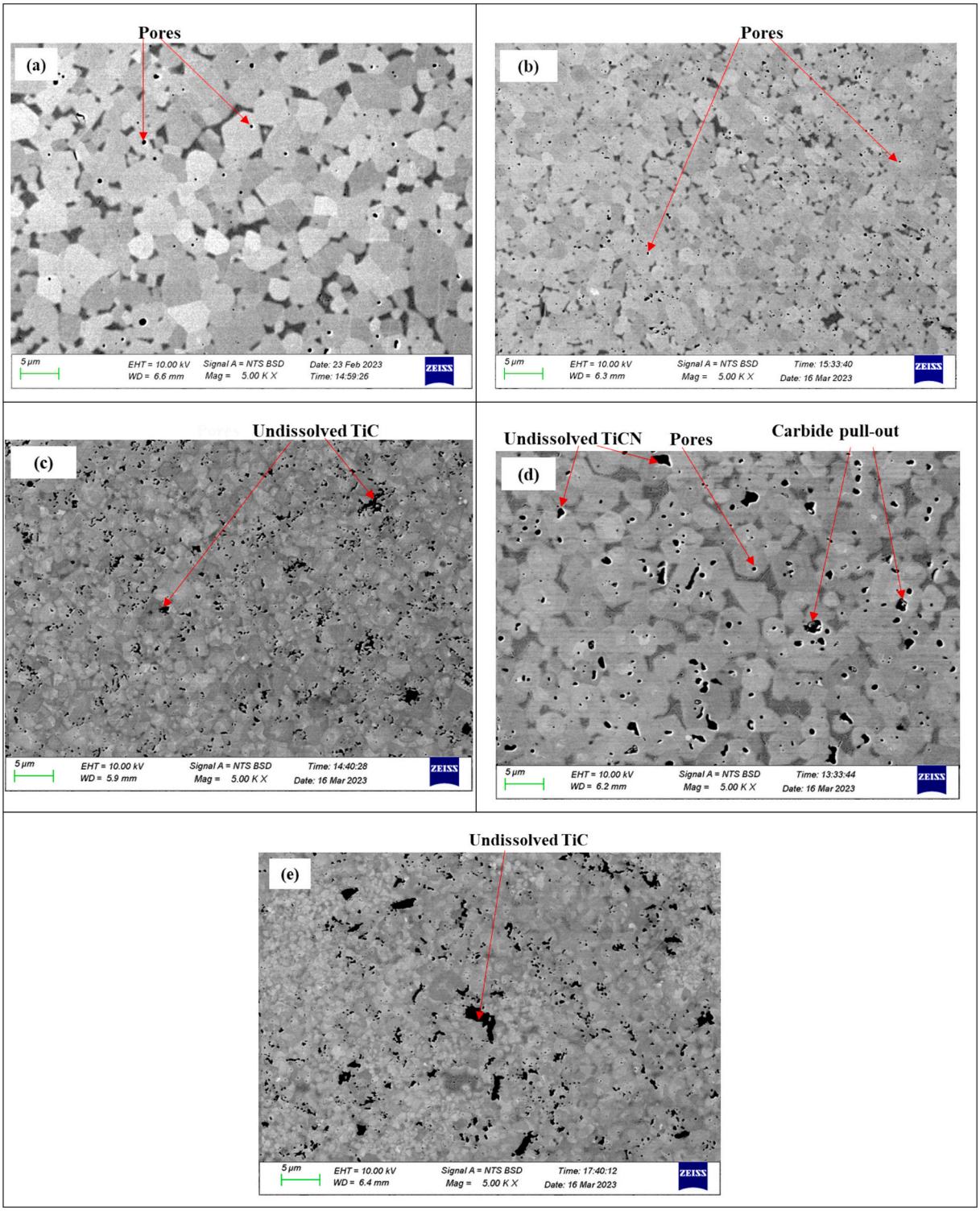

Fig. 2. SEM-BSE images of NbC-12[Ni/Mo] (wt%) prepared by (a) LPS and (b) PECS, NbC-10TiC-12Ni (wt%) prepared by (c) PECS, NbC-10TiC_7N_3-12Ni (wt%) prepared by (d) LPS, and NbC-10TiC-12[Ni/Mo] (wt%) prepared by (e) PECS showing NbC (light), Ni (medium dark), TiC_7N_3-rich (dark), and TiC-rich (darkest) phases.

[13]. In this study, the addition of Mo to the NbC-12Ni (wt%) had no significant influence on the microstructure of PECS NbC-12[Ni/Mo] (wt %) sample (see Fig. 2). However, there was poor distribution of Ni binder in the microstructure of the latter compared to the former, suggesting that sintering at 1285 °C partially occurred in the solid state. Hence, higher sintering temperatures and pressures were required [26].

The EDS analysis of LPS and PECS NbC-12[Ni/Mo] (wt%) samples detected Mo as a trace element due to low amount added of 3.6 wt% [27]. It has been reported elsewhere [7], that during sintering Mo_2C and Mo elements usually dissolve and re-precipitate inside NbC grains to form (Nb, Mo) C solid solutions in NbC-Ni systems. In contrast to Mo, the TiC and TiC_7N_3 secondary hard phase additions to the PECS NbC-12Ni (wt%) composition reduced the grain sizes due to grain growth inhibition during sintering [2,28]. Furthermore, these phases did not fully

dissolve in the PECS samples (see Fig. 2) due to lower sintering temperatures and time [4]. The addition of Mo plus TiC addition to the PECS NbC-12Ni (wt%) composition also resulted in the reduction of NbC grain sizes as shown in Fig. 2 (e). The PECS produced NbC-10TiC-12Ni (wt%) and NbC-10TiC-12[Ni/Mo] (wt%) samples exhibited very similar microstructural characteristics (see Figure Fig. 2 (c) and (d)). However, the PECS NbC-10TiC-12[Ni/Mo] (wt%) sample exhibited slightly pronounced poor distribution of Ni binder and increased amounts of undissolved TiC phases in its microstructure compared to the PECS NbC-10TiC-12Ni (wt%) sample. As a result, higher temperatures and pressures were required during the sintering process. Unlike with Mo, the microstructures of the LPS produced NbC-10TiC_7N_3-12Ni (wt%) sample exhibited small amounts of sparsely distributed undissolved TiC_7N_3 (represented by the dark contrast regions as confirmed by EDS mapping), as shown in Fig. 2 (d). Thus, most of these phases were dissolved in NbC grains during the LPS process, resulting in the formation of (Nb, Ti) (C, N) solid solutions [13,26]. In addition, the microstructure of LPS sample containing TiC_7N_3 secondary carbide phases exhibited carbide pull-outs. This was attributed to the abrasive effect of grinding and polishing during sample preparation [29].

3.3. Mechanical properties

The mechanical properties of the sintered samples are given in Table 5. Fig. 3 shows the relationship between the Vickers hardness and fracture toughness of the sintered samples. The LPS WC-10TiC-10[Co/Mo] (wt%) sample had the highest Vickers hardness (HV_{30}) (~14.5 GPa) compared to all the samples irrespective of composition or sintering technique. This was mainly due to the higher hardness of WC (22.5 GPa) compared to NbC (19.6 GPa) [30], Ni's lower hardness (or higher plasticity) than Co [2], and the finer WC grains within the LPS WC-10TiC-10[Co/Mo] (wt%) microstructure [2,5]. The additions of Mo and TiC_7N_3 to the NbC-12Ni (wt%) improved the hardness of NbC-12[Ni/Mo] (wt%) and NbC-10TiC_7N_3-12Ni (wt%) samples through the formation of the respective (Nb, Mo) C and (Nb, Ti) (C, N) solid solutions [31]. As shown in Fig. 3, there was no significant difference in the hardness properties of both LPS and PECS produced samples with NbC-12[Ni/Mo] (wt%) composition. This observation was consistent with the comparable densification and microstructures exhibited by the samples. The PECS produced NbC-10TiC_7N_3-12Ni (wt%) sample had a slightly higher hardness than its LPS counterpart (see Fig. 3). This was attributed to the smaller fine grains because of lower sintering temperatures and shorter sintering times in PECS than LPS [17], and the presence of slightly pronounced hard undissolved TiC_7N_3 grains in the PECS sample. The addition of a combination of Mo plus TiC to the NbC-12Ni (wt%) composition significantly improved the hardness properties in the PECS produced NbC-10TiC-12[Ni/Mo] (wt%) sample (Fig. 3). This was due to

Table 5
Mechanical properties of the sintered samples.

Samples Composition (wt%)	Vickers hardness, HV_{30} (GPa)	Fracture toughness, K_{IC} ($MPa.m^{1/2}$)	Elastic modulus, E (GPa)	Shear modulus, G (GPa)
WC-10TiC-10Co (LPS)	14.53 ± 0.13	8.83 ± 0.11	472.11 ± 0.37	183.55 ± 0.16
NbC-12[Ni/Mo] (LPS)	12.81 ± 0.12	6.99 ± 0.25	372.47 ± 1.84	149.85 ± 0.32
NbC-12[Ni/Mo] (PECS)	12.81 ± 0.58	6.09 ± 0.35	482.01 ± 0.42	198.32 ± 0.16
NbC-10TiC-12Ni (PECS)	13.06 ± 0.08	5.55 ± 0.08	547.54 ± 2.06	216.18 ± 0.12
NbC-10TiC-12 [Ni/Mo] (PECS)	14.11 ± 0.22	6.19 ± 0.24	479.19 ± 0.33	204.32 ± 0.04
NbC-10TiC_7N_3-12Ni (LPS)	12.77 ± 0.13	9.31 ± 0.53	429.16 ± 0.84	185.65 ± 0.07
NbC-10TiC_7N_3-12Ni (PECS)	13.70 ± 0.32	5.50 ± 0.06	549.60 ± 1.15	216.24 ± 0.21

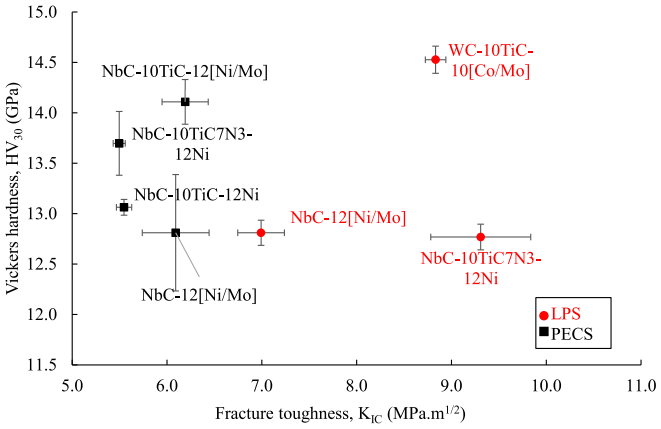

Fig. 3. Variation of Vickers hardness (HV_{30}) with fracture toughness (K_{IC}).

the combined effect of PECS's NbC grain refinement and the formation of (Nb, Mo, Ti) C solid solutions during sintering [31]. Furthermore, TiC has a hardness of ~30 GPa [6], thus, the presence of hard undissolved TiC in PECS NbC-10TiC-12[Ni/Mo] (wt%) sample's microstructure contributed to the increased hardness of the samples [6]. As shown in Fig. 3, the PECS NbC-10TiC-12[Ni/Mo] (wt%) sample exhibited the highest hardness (14.11 ± 0.22 GPa) among the NbC-Ni based samples. This was attributed to the combined effect of PECS and additions of Mo and TiC. The LPS produced NbC-10TiC_7N_3-12Ni (wt%) sample had the highest fracture toughness (K_{IC}) (9.31 ± 0.53) than all the other NbC-Ni based samples irrespective of composition and sintering technique (see Table 5 and Fig. 3). This was attributed to the more homogeneously distributed thicker and tougher (higher plasticity) Ni binder pools which acted as layers that inhibited crack propagation, as well as the slightly larger NbC grains [32]. The fine grained LPS WC-10TiC-10[Co/Mo] (wt%) sample had comparable K_{IC} (8.83 ± 0.11 $MPa.m^{1/2}$) to the LPS produced NbC-10TiC_7N_3-12Ni (wt%) sample. This was attributed to the homogeneous distribution of Co between the fine platelet (thin elongated) WC grains, and the relatively higher aspect ratio of the WC grains which has been found to improve fracture toughness in cemented carbides [33]. It is worth noting that usually, the fracture toughness of WC-Co alloys is directly proportional to the carbide grains sizes [34]. In general, the NbC-Ni based LPS produced samples exhibited higher fracture toughness (K_{IC}) than PECS produced samples with similar compositions (see Fig. 3). The higher K_{IC} in the LPS samples was due to the slightly larger NbC grains and the homogeneous distribution of the binder phase during LPS than in PECS [35]. The more homogeneous distribution of binder in LPS improved the carbide solubility, and the capillary action of the liquid during secondary re-arrangement stage of sintering, as well as reducing the amounts of carbide-to-carbide interfaces which are areas known to be prone to fracturing and are considered critical in cemented carbides fracture mechanics [32]. In contrast, during the PECS process, considerable inhomogeneous temperature distribution occurs from the centre to the surface of the conducting Ni particles when the pulsed current is carried through [36]. The Ni particles reach very high temperatures, melting momentarily, and the undergo rapid solidification [36], leading to poor binder distribution and carbide-to-carbide networks [7].

Fig. 4 shows the variation of the elastic modulus and Vickers hardness. The PECS produced samples exhibited relatively higher modulus of elasticity (E) and rigidity (G) compared to the LPS samples (see Fig. 4 and Table 5). The lower E and G in LPS samples was due to the presence of slightly larger and pronounced pores (defects) in the microstructures [13]. The LPS NbC-12[Ni/Mo] (wt%) sample had the lowest moduli properties compared to all the other samples irrespective of composition and sintering technique. This was attributed to the presence of "weak functions" of the carbide phase (i.e. (Nb, Mo) C solid solutions) that have

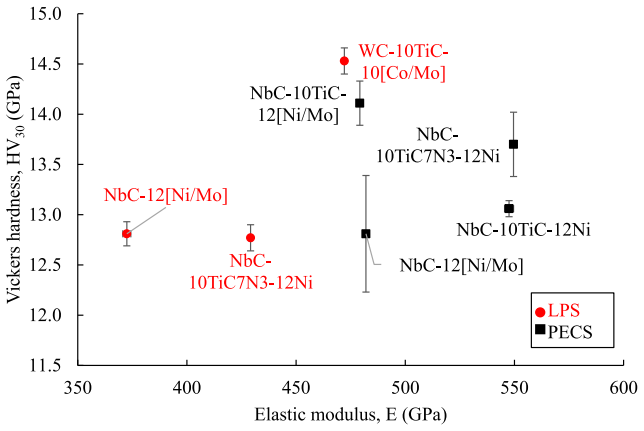

Fig. 4. Variation of elastic modulus (E) with the Vickers hardness (HV_{30}).

weak bonding strength [13,37], as well as porosity in the sample's microstructure. The presence of Mo in NbC-Ni systems results in the reduction of moduli properties [7]. In this study, Mo addition to the NbC-12Ni (wt%) composition had similar effects. This observation was confirmed by comparing the elastic and shear moduli of the PECS produced NbC-12[Ni/Mo] (wt%) and NbC-10TiC-12[Ni/Mo] (wt%) samples to the NbC-10TiC-12Ni (wt%) sample respectively (see Fig. 4 and Table 5). As shown in the figure, samples containing Mo had comparable elastic moduli properties which were lower than that of PECS NbC-10TiC-12[Ni/Mo] (wt%) sample. The LPS WC-10TiC-10Co (wt%) sample exhibited comparable moduli properties to the PECS produced NbC-12[Ni/Mo] (wt%) and NbC-10TiC-12[Ni/Mo] (wt%) samples. This was due to the presence of respective (W, Ti, Mo) C, (Nb, Mo) C and (Nb, Ti, Mo) C solid solutions in the samples [38]. The PECS produced NbC-10TiC_7N_3-12Ni (wt%) and NbC-10TiC-12Ni (wt%) samples exhibited the highest elastic and shear moduli (see Fig. 4 and Table 5) compared to all the other samples used in this study. This was attributed to the undissolved hard TiCN and TiC phases within the respective microstructures. The relatively higher E and G these samples suggested that the respective solid solutions formed through the respective additions of TiC_7N_3 and TiC have relatively stronger bonding strength than those containing Mo.

3.4. Face-milling machining performance

The machining performance of cutting inserts in face milling is heavily influenced by wear mechanisms that develop during operation. Mechanical wear, including abrasion, attrition, and fracture, along with chemical wear, such as diffusion, are the primary contributors to insert wear [4,39]. Flank wear, the most common type, results from the continuous rubbing between the insert cutting edge and the workpiece. This contact leads to abrasive and adhesive wear, especially at elevated temperatures where chemical reactions can further accelerate wear [2,39]. Abrasion, often identified by grooves aligned with the cutting direction, is the dominant mechanism driving flank wear [39]. Fig. 5 shows the optical micrographs of the flank and rake faces of PECS NbC-10TiC-12[Ni/Mo] (wt%) (a) S-LSM and (b) P-LSM, and (c) LPS WC-10TiC-10[Co/Mo] (wt%) cutting inserts' edges. As shown in the figure, the optical micrographs of the cutting inserts revealed that the main wear and cutting-edge failure mechanisms during machining of a-GCI were abrasion, attrition, and mechanical fracture which was characterised by cracks, chipping and edges shattering. Due to the brittle graphite flakes within the a-GCI workpiece, crater wear was not detected on the optical micrographs of the rake faces of all cutting inserts irrespective of composition, sintering technique or type of cutting edge [40]. Similarly, the optical micrographs did not reveal any workpiece built-up edge of the cutting inserts. To assess the machining performance, parameters such as the average resultant cutting force (F), cutting insert tool life (t), maximum flank wear (VB_{max}), and flank wear rate (FWR) were measured as shown in Table 6. These parameters were used to analyse and determine the machining performance of the cutting inserts. In addition, the effects of composition, sintering technique and cutting inserts edge designs (i.e. blank (B) or unmodified, shark skin (S-LSM), and pyramid (P-LSM)) were evaluated to investigate the machining performance of WC-Co and NbC-Ni based cutting inserts during machining of a-GCI.

3.4.1. Effects of composition and sintering on machining performance

The effects of composition and sintering process were evaluated using the unmodified (blank) cutting inserts. Among the blank inserts, the LPS produced WC-10TiC-10[Co/Mo] (wt%) (B) and NbC-10TiC_7N_3-12Ni (wt%) (B) cutting inserts achieved insert tool life of 20 min (see Table 6). Although both inserts demonstrated comparable performance, the LPS WC-10TiC-10[Co/Mo] (wt%) (B) insert exhibited slightly lower cutting force and FWR than the LPS NbC-10TiC_7N_3-12Ni (wt%) (B) insert. Notably, the LPS WC-10TiC-10[Co/Mo] (wt%) (B) insert achieved the lowest FWR (1.97 μm/min) among all blank cutting inserts, irrespective of composition or sintering process. The slightly better machining performance of the LPS WC-10TiC-10[Co/Mo] (wt%) (B) insert were attributed to the good combination of physical and mechanical properties of WC-Co based inserts [5]. The impact of composition was also evident in the PECS produced NbC-Ni cutting inserts. As shown in Table 6, the PECS NbC-10TiC-12Ni (wt%) (B) insert, containing TiC, demonstrated better machining performance (i.e. lower F and FWR, and slightly higher insert tool life (t)) compared to the PECS NbC-10TiC_7N_3-12Ni (wt%) (B) and PECS NbC-12[Ni/Mo] (wt%) inserts. While the PECS NbC-10TiC-12Ni (wt%) (B) and PECS NbC-10TiC_7N_3-12Ni (wt%) (B) inserts showed comparable performance, the PECS NbC-12[Ni/Mo] (wt%) exhibited significantly poorer results (i.e. insert tool life of 2 min, as well as highest FWR (21.04 μm/min, and F (1358 N)). The slightly better performance of TiC and TiC_7N_3 containing inserts was attributed to the enhanced hardness due to the presence of the undissolved TiC and TiC_7N_3 phases within the inserts' microstructures, resulting in improved resistance to abrasion wear [4]. Furthermore, the inserts had relatively higher elastic modulus (see Fig. 4) which improved the stiffness of the cutting inserts and resistance to deformation under the forces generated during cutting. The sintering process also impacted the performance of NbC-Ni based cutting inserts. For example, the LPS produced NbC-12[Ni/Mo] (wt%) (B) and NbC-10TiC_7N_3-12Ni (wt%) (B) inserts exhibited better insert tool life performance than their PECS counterparts. This improvement was attributed to the relatively higher K_{IC} of LPS produced inserts which enhanced impact resistance and reduced cutting edge wear and failure by mechanical fracture during machining [35].This finding underscores that machining performance of conventionally sintered NbC-Ni based inserts could be improved through the additions of Mo and TiC_7N_3 to offer comparable performance to WC-Co based inserts.

3.4.2. Effects of fs-LSM on machining performance

The impact of LSM was analysed by comparing the unmodified inserts with LSM-treated inserts. Laser surface modification had negligible impact on the tool life of WC-10TiC-10[Co/Mo] (wt%) (B) insert in terms of cutting time since all inserts achieved 20 min cutting time (see Table 6). Notably, the LSM treatment increased the average resultant cutting force by more than 80 N for both LPS WC-10TiC-10[Co/Mo] (wt %) S-LSM and LPS WC-10TiC-10[Co/Mo] (wt%) P-LSM inserts (see Table 6). Furthermore, the LPS WC-10TiC-10[Co/Mo] (wt%) P-LSM insert exhibited slightly lower FWR (1.78 μm/min) compared to the B counterpart, whereas the S-LSM insert showed the opposite trend. It is still not clearly understood why the inserts exhibited this behavior, and further investigations are underway to better understand this phenomenon.

Regarding the NbC-Ni based cutting inserts, LSM improved the insert tool life performance of all the inserts except for the LPS NbC-10TiC_7N_3-

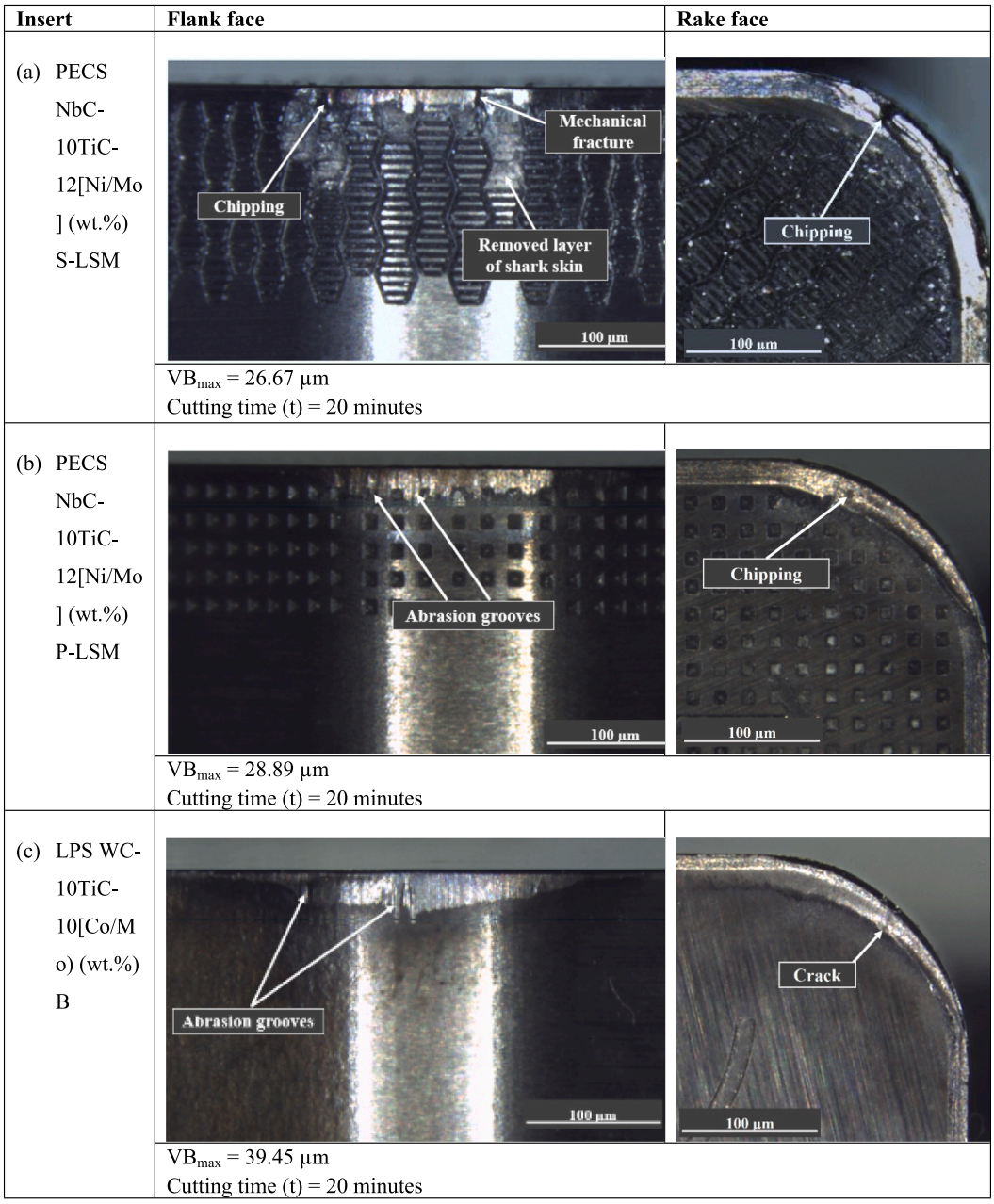

Fig. 5. Optical micrographs of the flank and rake faces of PECS NbC-10TiC-12[Ni/Mo] (wt%) (a) S-LSM and (b) P-LSM, and (c) LPS WC-10TiC-10[Co/Mo] (wt%) cutting inserts' edges during machining.

12Ni (wt%) B cutting insert (see Table 6). The LSM treatment improved the insert tool life performances, reducing FWRs of all PECS cutting inserts. For instance, the S-LSM resulted in insert tool improvements of 300 %, 233 %, and 150 % for cutting inserts with compositions NbC-12[Ni/Mo] (wt%), NbC-10TiC$_7$N$_3$-12Ni (wt%), and NbC-10TiC-12Ni (wt %), respectively (see Fig. 6). Similarly, the P-LSM improved the insert tool life of inserts with similar compositions by 900 %, 233 % and 150 %, respectively (see Fig. 7). The insert tool life improvements and the consequent FWRs reductions were attributed to the improved surface hardness, cutting edge strengthening and abrasive wear resistance [41].

The machining performances of LSM treated inserts were comparable to one another, irrespective of composition (see Table 6). However, with the exception of the PECS NbC-10TiC-12[Ni/Mo] (wt%) S-LSM insert, the P-LSM inserts, generally demonstrated slightly better performance than their S-LSM counterparts. For instance, the P-LSM cutting inserts exhibited slightly lower average resultant cutting forces (F) and flank wear rates (FWRs) compared to the S-LSM cutting inserts. This indicates that pyramid micro-textures were generally more effective in enhancing machining performance than shark skin micro-textures. This observation aligns with findings from previous investigations [41–43], which have noted that pyramid based micro-textures can reduce the chip-tool contact length, decrease friction and improve insert tool life performance.

Overall, the PECS NbC-10TiC-12[Ni/Mo] (wt%) inserts had the best machining performance after the LSM treatment. For example, the PECS NbC-10TiC-12[Ni/Mo] (wt%) S-LSM insert had the lowest flank wear rate (FWR) (1.33 µm/min) among all the inserts with maximum flank wear (VB_{max}) of 26.67 µm after 20 min of machining. This was followed closely by the P-LSM insert of similar composition with FWRs of 1.44 µm/min after 20 min of machining. These NbC-Ni based inserts outperformed the WC-Co based LPS WC-10TiC-10[Co/Mo] B insert which had a FWR 1.97 µm/min after 20 min of machining respectively (see

Table 6
Inserts properties for different cutting edges.

		Insert number						
		1	2	3	4	5	6	7
Type of Edge	Properties	WC-10TiC-10 [Co/Mo] (LPS)	NbC-12[Ni/Mo] (LPS)	NbC-12[Ni/Mo] (PECS)	NbC-10TiC-12Ni (PECS)	NbC-10TiC-12[Ni/Mo] (PECS)	NbC-10TiC$_7$N$_3$-12Ni (LPS)	NbC-10TiC$_7$N$_3$-12Ni (PECS)
Blank (B)	F (N)	669	833	1358	609	Damaged	838	793
	t (min)	20	11	2	8	Damaged	20	6
	VBmax (μm)	39.45	34.45	42.07	24.45	Damaged	76.11	37.39
	FWR (μm/min)	1.97	3.13	21.04	3.06	Damaged	3.81	6.23
Shark skin (S-LSM)	F (N)	756	793	853	854	881	1141	918
	t (min)	20	20	8	20	20	14	20
	VBmax (μm)	50	63.89	47.78	46.67	26.67	87.75	46.67
	FWR (μm/min)	2.50	3.19	5.97	2.33	1.33	6.27	2.33
Pyramid (P-LSM)	F (N)	763	742	744	733	706	844	801
	t (min)	20	17	20	20	20	14	20
	VBmax (μm)	35.56	44.45	38.89	36.67	28.89	54.45	60.56
	FWR (μm/min)	1.78	2.61	1.94	1.83	1.44	3.89	3.03

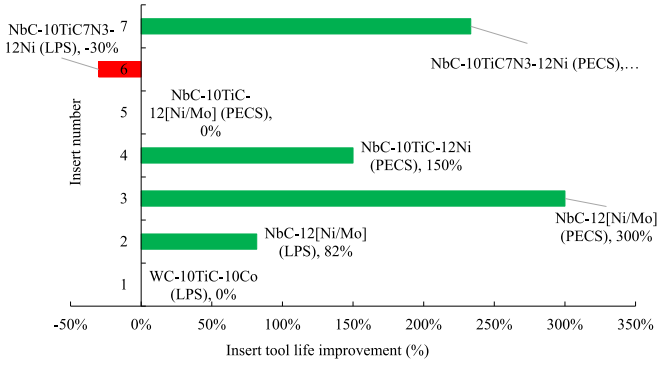

Fig. 6. Effect of shark skin (S-LSM) technique on the cutting insert life performance benchmarked against blank (B) cutting inserts during machining.

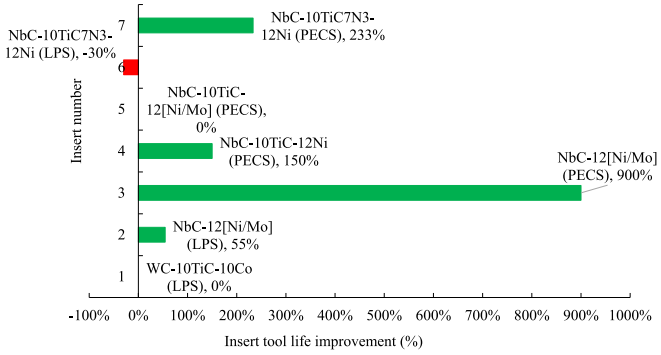

Fig. 7. Effect of pyramid (P-LSM) technique on the cutting insert life performance benchmarked against blank (B) cutting inserts during machining.

Table 6). The low FWRs in the PECS NbC-10TiC-12[Ni/Mo] (wt%) S-LSM and P-LSM inserts were attributed to the improved surface hardness and strengthening of the cutting-edge due to a formation of a LSM self-carbide coating layer [4]. In contrast, the slightly poor performance of LPS WC-10TiC-10[Co/Mo] B insert was attributed to the chemical instability of WC-Co based inserts during the machining of a-GCI, as iron's higher affinity for carbon is higher than that of WC) [5]. The machining performance of the PECS NbC-10TiC-12[Ni/Mo] (wt%) LSM inserts suggests that a combination of TiC and Mo is a more effective additive to NbC-Ni compositions than using TiC or TiCN alone.

Fig. 8 shows the HAADF-STEM mapping of PECS NbC-10TiC-12[Ni/Mo] (wt%) S-LSM insert cutting edge/workpiece interface. The figure shows that the insert exhibited an overlap between Nb, Ti and Mo elements (indicating the formation of the hard (Nb, Ti, Mo) C solid solution) toward the cutting edge due to LSM application. This solid solution, which plays a critical role in in hardness, is influenced by the binder [44]. The figure suggests that the cutting edge is primarily composed of the (Nb, Ti, Mo) C solid solution, implying high hardness and improved abrasion wear resistance. Furthermore, the TiC appears to be fully dissolved in this layer, unlike in the sample or bulk microstructure. This dissolution enhances the surface hardness and improves abrasion wear resistance, resulting in lower FWR [2]. A similar observation was made in a different study [4] whereby the application of a femtosecond LSM technique was reported to have produced a "hard" ~2.5 μm thick "self-carbide" coating on the surface of the cutting edge. Although the LSM techniques generally improved machining performance, however, it was observed that in the NbC-10TiC$_7$N$_3$-12Ni (wt%) (B) insert produced by LPS, both LSM techniques reduced the tool life. The reasons for this are not fully understood, and the varying effects of LSM underscore the nuanced impact of the technique. This highlights the need for further studies and a comprehensive understanding of the material-specific interactions to optimise its application.

4. Conclusions

Pulsed electric current sintering (PECS) resulted in higher hardness than liquid phase sintering (LPS). Due to the higher hardness of WC (22.5 GPa) compared to NbC (19.6 GPa), and Ni's lower hardness (or higher plasticity) than Co, the LPS WC-10TiC-10[Co/Mo] (wt%) sample had the highest hardness compared to all the NbC-Ni based samples irrespective of composition or sintering technique. The additions of Mo, TiC, TiC$_7$N$_3$, and a combination of Mo and TiC to the NbC-12Ni (wt%) composition significantly improved the hardness properties in all PECS samples. The LPS produced NbC-10TiC$_7$N$_3$-12Ni (wt%) sample had the highest fracture toughness (K_{IC}) among the NbC-Ni based samples. Molybdenum addition to the NbC-Ni based cemented carbides resulted in the reduction of the elastic modulus (E) and shear rigidity (G). Due to the presence of the undissolved hard TiCN and TiC phases within the microstructure, the PECS produced NbC-10TiC$_7$N$_3$-12Ni (wt%) and NbC-10TiC-12Ni (wt%) samples exhibited the highest E and G compared to all the other samples used in this study. Face milling tests on the blank (unmodified) cutting inserts indicated that additions of Mo and TiC$_7$N$_3$ to the conventionally sintered NbC-Ni inserts can significantly improve mechanical properties and resistance to abrasion wear, achieving performance comparable to the WC-Co based inserts. Laser surface

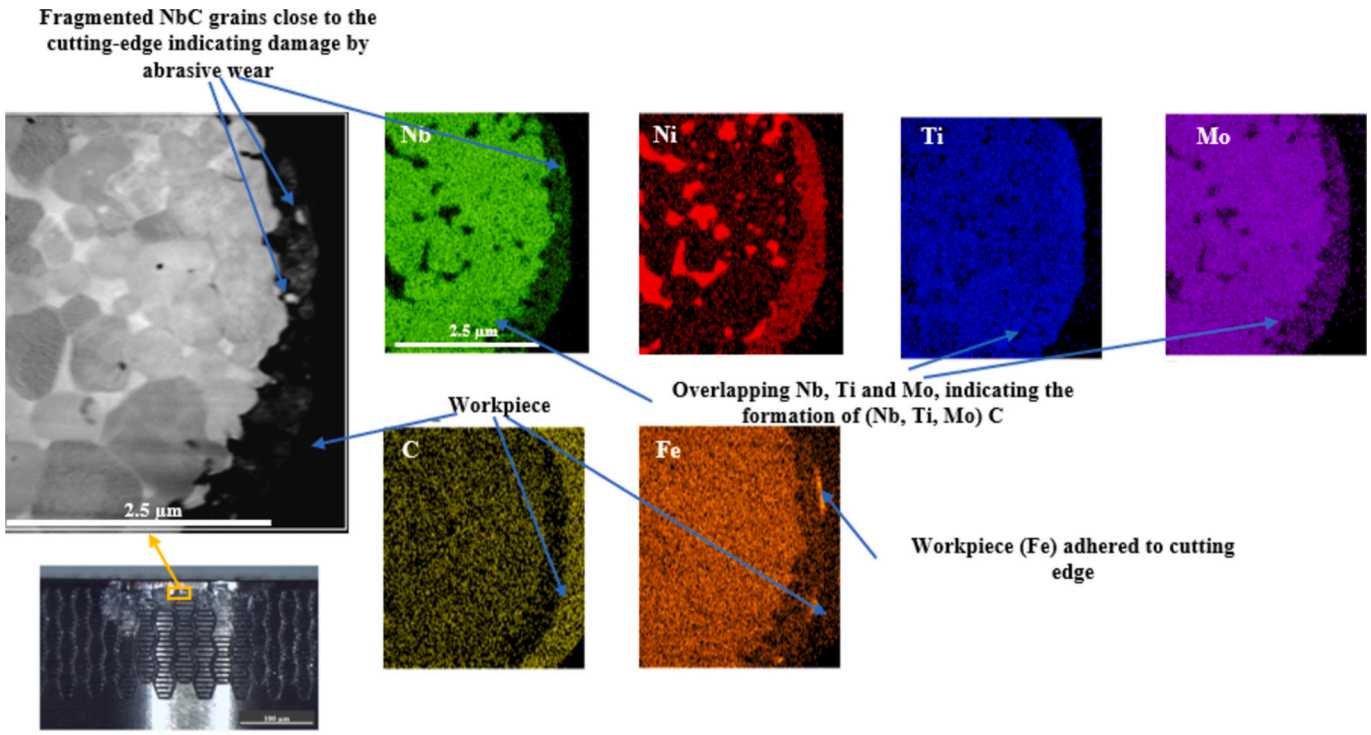

Fig. 8. HAADF-STEM map of a cross-section of PECS NbC-10TiC-12[Ni/Mo] (wt%) S-LSM cutting edge/workpiece interface showing: Nb (green), Ni (red), Ti (blue), Mo (purple), C (yellow), and Fe (orange). (For interpretation of the references to colour in this figure legend, the reader is referred to the web version of this article.)

modification (LSM) improved the surface hardness and the overall machining performance of NbC-Ni cutting inserts. During machining, the PECS NbC-10TiC-12[Ni/Mo] (wt%) S-LSM insert had the lowest flank wear rate (FWR) after a cutting time of 20 min, followed by the P-LSM insert with similar composition. The good machining performance of PECS NbC-10TiC-12[Ni/Mo] (wt%) S-LSM and P-LSM inserts was attributed to the formation of (Nb, Ti, Mo) C solid solution toward the cutting edge due to LSM treatment. Although LSM improved the abrasive wear resistance and increased insert tool life performance of PECS produced NbC-10TiC_7N_3-12Ni (wt%) based inserts, adverse effects were observed on the LPS produced NbC-12Ni (wt%) inserts. Overall, this study demonstrated that through careful composition design, optimised sintering process, and laser surface modification, the NbC-Ni based cutting inserts can achieve comparative performance to WC-Co based inserts.

CRediT authorship contribution statement

M. Rabothata: Writing – original draft, Visualization, Project administration, Methodology, Formal analysis, Data curation, Conceptualization. **R. Genga:** Writing – review & editing, Conceptualization. **N. Mphasha:** Project administration, Methodology, Investigation. **K. Phaka:** Resources, Methodology, Investigation. **N. Nelwalani:** Visualization. **S. Ngongo:** Visualization. **C. Polese:** Writing – review & editing, Project administration, Investigation. **S. Huang:** Resources, Conceptualization. **J. Vleugels:** Conceptualization. **P. Zeman:** Resources.

Declaration of competing interest

The authors declare that they have no known competing financial interests or personal relationships that could have influenced the work reported in this paper.

Data availability

The data that has been used is confidential.

Acknowledgements

This work was financially supported by SITA Air Transport Community Foundation and DSI-NRF Centre of Excellence in Strong Materials (CoE-SM Grant No: 41292). The authors would also like to thank Auto Industrial group (AIG) (Pty) Ltd., and Mr. James Shepperd for donating the automotive grey cast iron (a-GCI) workpieces used for machining.

References

[1] M.O. Genç, Ç. Imer, Graphite flake size effects to thermal durability of automobile flywheel under forced slippage, in: Proceedings of the World Congress on Mechanical, Chemical, and Material Engineering, 2017, pp. 1–8, https://doi.org/10.11159/icmie17.121.
[2] G.S. Upadhyaya, D.R. Tobergte, S. Curtis, Cemented Tungsten Carbides: Production, Properties, and Testing, Indian Institute of Technology, Kanpur, India, 1998, https://doi.org/10.1016/B978-081551417-6.50015-0.
[3] A. Rizzo, et al., The critical raw materials in cutting tools for machining applications: a review, Materials 13 (6) (2020) 1–48, https://doi.org/10.3390/ma13061377.
[4] R.M. Genga, et al., Roughing, semi-finishing and finishing of laser surface modified nickel bonded NbC and WC inserts for grey cast iron (GCI) face-milling, Int. J. Refract. Met. Hard Mater. 86 (June) (2019) 2020, https://doi.org/10.1016/j.ijrmhm.2019.105128.
[5] R.M. Genga, L.A. Cornish, M. Woydt, A. Janse van Vuuren, C. Polese, Microstructure, mechanical and machining properties of LPS and SPS NbC cemented carbides for face-milling of grey cast iron, Int. J. Refract. Met. Hard Mater. 73 (January) (2018) 111–120, https://doi.org/10.1016/j.ijrmhm.2017.12.036.
[6] K. Sarin, D. Mari Vinod, L. Llanes, Comprehensive Hard Materials, Elsevier, Oxford UK, 2014.
[7] R.M. Genga, L.A. Cornish, G. Akdogan, Effect of Mo2C additions on the properties of SPS manufactured WC-TiC-Ni cemented carbides, Int. J. Refract. Met. Hard Mater. 41 (2013) 12–21, https://doi.org/10.1016/j.ijrmhm.2013.01.008.
[8] G. Casalino, A.M. Losacco, A. Arnesano, F. Facchini, M. Pierangeli, C. Bonserio, Statistical analysis and modelling of an Yb: KGW femtosecond laser Micro-drilling process, Procedia CIRP 62 (2017) 275–280, https://doi.org/10.1016/J.PROCIR.2016.06.111.
[9] S. Fang, R. Lima, D. Sandoval, D. Bähre, L. Llanes, Ablation investigation of cemented carbides using short-pulse laser beams, Procedia CIRP 68 (April) (2018) 172–177, https://doi.org/10.1016/j.procir.2017.12.042.

[10] S.G. Huang, K. Vanmeensel, H. Mohrbacher, M. Woydt, J. Vleugels, Microstructure and mechanical properties of NbC-matrix hardmetals with secondary carbide addition and different metal binders, Int. J. Refract. Met. Hard Mater. 48 (2015) 418–426, https://doi.org/10.1016/j.ijrmhm.2014.10.014.
[11] D.K. Shetty, I.G. Wright, P.N. Mincer, A.H. Clauer, Indentation fracture of WC-co cermets, J. Mater. Sci. 20 (5) (1985) 1873–1882, https://doi.org/10.1007/BF00555296.
[12] ISO, "3685: Tool-life testing with single-point turning tools," 1993.
[13] R.M. Genga, et al., High-temperature sliding wear, elastic modulus and transverse rupture strength of Ni bonded NbC and WC cermets, Int. J. Refract. Met. Hard Mater. 87 (2020) 105143, https://doi.org/10.1016/j.ijrmhm.2019.105143.
[14] X. Wang, H.E. Xiaoxiang, G. Hailiang, Influence of Mo on the microstructure and mechanical properties of TiC-based cermets, Rare Metals 29 (4) (2010) 346, https://doi.org/10.1007/s12598-010-0127-y.
[15] R.M. Genga, et al., Effects of Mo2C, Ni binder and laser surface modification on WC inserts for turning Ti-6Al-4V, Int. J. Refract. Met. Hard Mater. 87 (2020) 105145, https://doi.org/10.1016/j.ijrmhm.2019.105145.
[16] D. Hübler, T. Gradt, Effect of different binders and secondary carbides on NbC cermets, Forschung im Ingenieurwesen/Engineering Research 86 (2) (2022) 197–211, https://doi.org/10.1007/S10010-022-00583-1/FIGURES/12.
[17] R.M. Genga, G. Akdogan, J.E. Westraadt, L.A. Cornish, Microstructure and material properties of PECS manufactured WC-NbC-CO and WC-TiC-Ni cemented carbides, Int. J. Refract. Met. Hard Mater. 49 (1) (2015) 240–248, https://doi.org/10.1016/j.ijrmhm.2014.07.030.
[18] Y. Li, N. Liu, X. Zhang, C. Rong, Effect of Mo addition on the microstructure and mechanical properties of ultra-fine grade TiC–TiN–WC–Mo2C–co cermets, Int. J. Refract. Met. Hard Mater. 26 (3) (2008) 190–196, https://doi.org/10.1016/J.IJRMHM.2007.05.005.
[19] S. Kim, S.H. Han, J.K. Park, H.E. Kim, Variation of WC grain shape with carbon content in the WC–co alloys during liquid-phase sintering, Scr. Mater. 48 (5) (2003) 635–639, https://doi.org/10.1016/S1359-6462(02)00464-5.
[20] G. Andersson, B. Jansson, The solubility of cubic carbide formers in liquid cobalt, in: G. Kneringer, P. Rodhammer, H. Wildner (Eds.), In *15th International Plansee Seminar*, Plansee Holding AG, Reutte, 2001.
[21] S.G. Huang, J. Vleugels, H. Mohrbacher, M. Woydt, Microstructure and mechanical properties of NbC matrix cermets using Ni containing metal binder, Metal Powder Report 71 (5) (2016) 349–355, https://doi.org/10.1016/j.mprp.2016.05.009.
[22] R.M. Genga, G. Akdogan, J.E. Westraadt, L.A. Cornish, Microstructure and material properties of PECS manufactured WC-NbC-CO and WC-TiC-Ni cemented carbides, Int. J. Refract. Met. Hard Mater. 49 (1) (2015) 240–248, https://doi.org/10.1016/j.ijrmhm.2014.07.030.
[23] J.H. Huang, S.G. Huang, P. Zhou, B. Lauwers, J. Qian, J. Vleugels, Microstructure and mechanical properties of WC or Mo2C modified NbC-Ni cermets, Int. J. Refract. Met. Hard Mater. 95 (2021) 105440, https://doi.org/10.1016/J.IJRMHM.2020.105440.
[24] M. Labonne, et al., Sintering behavior and microstructural evolution of NbC-Ni cemented carbides with Mo2C additions, Int. J. Refract. Met. Hard Mater. 92 (2020) 105295, https://doi.org/10.1016/J.IJRMHM.2020.105295.
[25] R.M. Genga, Microstructure and Properties of Selected Wc-Cemented Carbides Manufactured by Sps Method, University of Witwatersrand, 2014.
[26] S.G. Huang, J. Vleugels, H. Mohrbacher, M. Woydt, NbC grain growth control and mechanical properties of Ni bonded NbC cermets prepared by vacuum liquid phase sintering, Int. J. Refract. Met. Hard Mater. 72 (2018) 63–70, https://doi.org/10.1016/J.IJRMHM.2017.12.013.
[27] A. Ul-Hamid, A Beginners' Guide to Scanning Electron Microscopy, Springer Nature, Switzerland, 2018.
[28] R. Warren, Microstructural development during the liquid-phase sintering of two-phase alloys, with special reference to the NbC/co system, J. Mater. Sci. 3 (1968) 471–485.
[29] J. Hegeman, Jt. De Hosson, G. de With, Grinding of WC-co hardmetals, Wear 248 (2001) 187–196.
[30] T.W. Penrice, Alternative Binders for Hard Metals, Carbide Tool J. 20 (4) (1988) 12–15.
[31] S.G. Huang, et al., Microstructure and mechanical properties of (Nb,W,Ti)(C,N)-Ni solid solution cermets with 6 to 20 wt% Ni, Int. J. Refract. Met. Hard Mater. 103 (2022) 105757, https://doi.org/10.1016/J.IJRMHM.2021.105757.
[32] J.L. Chermant, F. Osterstock, Fracture Toughness and Fracture of WC-co Composites, 1976.
[33] L. Zhang, et al., Fine platelet-like grained WC–co cemented carbides: preparation, characterization, properties and application in PVD coating substrates, Int. J. Refract. Met. Hard Mater. 64 (2017) 135–142, https://doi.org/10.1016/j.ijrmhm.2017.01.015.
[34] C. Qian, K. Li, X. Yi Guo, B. Liu, Z. Yi Long, Y. Liu, Effect of WC grain size on mechanical properties and microstructures of cemented carbide with medium entropy alloy co-Ni-Fe binder, J. Cent. South Univ. 27 (4) (Apr. 2020) 1146–1157, https://doi.org/10.1007/S11771-020-4355-5/METRICS.
[35] R.M. Genga, G. Akdogan, C. Polese, J.C. Garrett, L.A. Cornish, Abrasion wear, thermal shock and impact resistance of WC-cemented carbides produced by PECS and LPS, Int. J. Refract. Met. Hard Mater. 49 (1) (2015) 133–142, https://doi.org/10.1016/j.ijrmhm.2014.07.031.
[36] M. Tokita, Spark plasma sintering (SPS) method, systems, and applications, in: Handbook of Advanced Ceramics: Materials, Applications, Processing, and Properties, Second Edi., Elsevier Inc., 2013, pp. 1149–1177, https://doi.org/10.1016/B978-0-12-385469-8.00060-5.
[37] S.R. Agnew, L. Dong, J.I. Keene, H.N.G. Wadley, Mechanical properties of large TiC-Mo-Ni cermet tiles, Int. J. Refract. Met. Hard Mater. 75 (2018) 238–247, https://doi.org/10.1016/J.IJRMHM.2018.05.005.
[38] Y. Mishima, S. Ochiai, N. Hamao, M. Yodogawa, T. Suzuki, Solid Solution Hardening of Nickel-Role of Transition Metal and B-Subgroup Solutes, 1986.
[39] A. Senthil Kumar, A. Raja Durai, T. Sornakumar, The effect of tool wear on tool life of alumina-based ceramic cutting tools while machining hardened martensitic stainless steel, J. Mater. Process. Technol. 173 (2) (2006) 151–156, https://doi.org/10.1016/J.JMATPROTEC.2005.11.012.
[40] R. C. Voigt, R. O. Marwanga, and P. H. Cohen, "Machinability of gray iron—mechanics of chip formation," *doi:* https://doi.org/10.1080/13640461.1999.11819335, vol. 11, no. 6, pp. 567–572, 1999, https://doi.org/10.1080/13640461.1999.11819335.
[41] N.T. Alagan, T. Beno, P. Hoier, U. Klement, A. Wretland, Influence of surface features for increased heat dissipation on tool wear, Materials 11 (5) (Apr. 2018), https://doi.org/10.3390/ma11050664.
[42] N. Tamil Alagan, P. Zeman, P. Hoier, T. Beno, U. Klement, Investigation of micro-textured cutting tools used for face turning of alloy 718 with high-pressure cooling, J. Manuf. Process. 37 (2019) 606–616, https://doi.org/10.1016/J.JMAPRO.2018.12.023.
[43] A. Salem, H. Hegab, H.A. Kishawy, Experimental investigation of the derivative cutting when machining AISI 1045 with Micro-textured cutting tools, Metals (Basel) 13 (9) (2023), https://doi.org/10.3390/met13091587.
[44] S.G. Huang, et al., Microstructure and mechanical properties of (Nb,W,Ti)(C,N)-Ni solid solution cermets with 6 to 20 wt% Ni, Int. J. Refract. Met. Hard Mater. 103 (2022) 105757, https://doi.org/10.1016/J.IJRMHM.2021.105757.